



**Anisotropic Manganese Antimonide Nanoparticle Formation
by Solution-Solid-Solid Growth Mechanism : Consequence of
Sodium Borohydride Addition Towards Reduced Surface
Oxidation and Enhanced Magnetic Moment**

Journal:	<i>Nanoscale</i>
Manuscript ID	NR-ART-11-2018-009142.R1
Article Type:	Paper
Date Submitted by the Author:	14-Feb-2019
Complete List of Authors:	Hettiarachchi, Malsha; Wayne State University, Department of Chemistry Abdelhamid, Ehab; Wayne State University, Nadgorny, Boris; Wayne State University, Physics & Astronomy Brock, Stephanie; Wayne State University, Department of Chemistry



Journal Name

ARTICLE

Anisotropic Manganese Antimonide Nanoparticle Formation by Solution-Solid-Solid Growth Mechanism : Consequence of Sodium Borohydride Addition Towards Reduced Surface Oxidation and Enhanced Magnetic Moment

Received 00th January 20xx,
Accepted 00th January 20xx

DOI: 10.1039/x0xx00000x

www.rsc.org/

Malsha A. Hettiarachchi^a, Ehab Abdelhamid^b, Boris Nadgorny^b and Stephanie L. Brock^{*a}

A new approach to the solution-phase synthesis of manganese antimonide nanoparticles was developed to reduce competitive oxide formation by exploitation of sodium borohydride (NaBH₄) (0.53-2.64 mmol) as a sacrificial reductant. However, in the presence of near-stoichiometric precursor amounts of manganese carbonyl and triphenyl antimony, the introduction of NaBH₄ results in a different growth mechanism, Solution-Solid-Solid (SSS), leading to tadpole-shaped manganese antimonide nanoparticles with antimony-rich heads and stoichiometric manganese antimonide tails. We hypothesize that a solid antimony-rich manganese antimonide cluster acts as an initiator to tail growth in solution. Notably, the length of the “tail” correlated with the amount of NaBH₄ used. Interestingly, these anisotropic particles can be transformed progressively into spherical-shaped nanoparticles upon the addition of excess manganese carbonyl. The anisotropic manganese antimonide particles possess saturation magnetizations ca. twenty times higher than that reported for MnSb nanoparticles prepared without NaBH₄, attributed to limitation of oxidation.

Introduction

Bulk MnSb, and related ternary phases, have long been studied due to the strong coupling between the ferromagnetic properties and caloric, optical (Kerr effect) and/or structural changes, achievable near room temperature. Therefore, these phases are of interest as potential magnetic refrigerant materials,¹ and components in data storage/processing devices² and magneto-optical readouts.³

Nano-structures of MnSb have also been investigated, as epitaxial dots grown on supporting substrates including Si⁴ and GaAs³, and as thin films on Ge/Si⁵. MnSb nanoparticles on Si (111) with lateral diameter $\langle d \rangle < 9$ nm were found to exhibit superparamagnetic properties while MnSb nanoparticles with $\langle d \rangle \geq 15$ nm are ferromagnetic at room temperature.⁴ For GaAs, the cluster coalescence of MnSb nano dots (nominal thickness 0.35-1.05 nm) leads to an increased saturation magnetization compared to thin films of MnSb (thickness 5 nm), and polar magnetic dichroism, an indication of the active magneto-optical properties of these MnSb dots.³ Finally, in the case of molecular beam epitaxial growth of 70 nm thickness MnSb (0001) films on Ge (111)/Si (111) by reduced pressure vapour deposition, a saturation magnetization value of 3.3 BM/Mn⁵, approaching

^a Department of Chemistry, Wayne State University, Detroit, MI 48202; United States, email: sbrock@chem.wayne.edu

^b Department of Physics and Astronomy, Wayne State University, Detroit, MI 48201, United States

Electronic Supplementary Information (ESI) available: HAADF-STEM and EDS mapping, Powder X-Ray Diffraction patterns, Transmission Electron Microscopy images of the products obtained under various conditions. See DOI: 10.1039/x0xx00000x

the experimentally recorded moment for bulk MnSb (3.5 BM/Mn)⁶ is achieved.

The Brock group has pioneered the synthesis of MnSb nanoparticles by solution phase routes.⁷ Growing nanocrystals in the solution phase evades strain induced in the nanoparticles due to epitaxial supports, enabling the study of intrinsic size and shape-dependent properties. In this method of synthesizing MnSb nanoparticles, the driving factor for the successful preparation of MnSb with no evident precipitation of elemental antimony (Sb) as a secondary phase, was to use a large excess of manganese (Mn) precursor, manganese carbonyl [Mn₂(CO)₁₀] (*ca.* 160% mole Mn excess). We rationalized the need for excess Mn₂(CO)₁₀ as a function of the high volatility of Mn₂(CO)₁₀ in the reaction at elevated temperatures. In addition, we observed a manganese oxide (MnO_x) shell around the MnSb nanoparticle core, which we suspected formed because of an adventitious oxygen source. This MnO_x shell formation not only consumes a portion of the Mn₂(CO)₁₀, resulting in Mn precursor deficiency relative to triphenyl antimony (Ph₃Sb), but also reduces the magnetic moment of the material when calculated with respect to the Mn moles in the final product (0.04 BM/MnSb vs. 3.3 BM/MnSb for bulk). We presume that when excess Mn₂(CO)₁₀ is present, it acts as a sacrificial agent to react with adventitious oxygen producing free MnO_x that washes away in the purification process, in addition to forming an amorphous shell around the MnSb core. Further, we hypothesized that a reducing agent would be a stronger sacrificial agent (better oxygen-getter) than Mn₂(CO)₁₀ and could react quickly with adventitious oxygen before it reacts with Mn₂(CO)₁₀, thus reducing or eliminating the excess Mn₂(CO)₁₀ for the reaction and the extent of oxidation.

To test this hypothesis, we employed a mild reducing agent, sodium borohydride (NaBH₄), in the synthesis, and in so doing revealed a new mechanism for MnSb formation based on the Solution-Solid-Solid (SSS) mechanism. SSS growth has become a prominent synthetic strategy for synthesizing one dimensional (1-D) semiconductor nanorods and nanowires in solution, such as ZnSe⁸⁻¹⁰ and CdSe^{8,11-13}. In SSS, a solid particle acts as an active catalyst, facilitating the

formation of tail growth by breaking down precursor components in the solution phase. This mechanism is distinguished from the more common Solution-Liquid-Solid (SLS) growth mechanism by the use of nucleating particles with bulk melting points several hundred degrees above the reaction temperature.^{8-10, 14-19} In general, nucleating nanoparticles are superionic in character, and the growth is vacancy driven. However, Buhro and co-workers have observed the same growth pattern for CdTe when Bi nanoparticles are employed, with Bi₂Te₃ identified as the “active catalyst”. SSS has also proven to be a model method to synthesize complex ternary and quaternary nanowires and nanoribbons such as CuInS₂,¹⁶ CuGaS_xSe_{2-x},²⁰ and AgInZn₇S₉,²¹ which are challenging to prepare by conventional reaction approaches. To the best of our knowledge, the use of antimonides as catalysts for SSS has not been reported.

Experimental

Materials

Mn₂(CO)₁₀ (98%), Ph₃Sb (99%), NaBH₄ (90%) 1-octadecene (1-ODE) (90%, technical grade) and trioctylphosphine oxide (TOPO) (90%, technical grade) were purchased from Sigma Aldrich, Inc. Chloroform was purchased from Fisher Scientific, and ethanol (200 proof) was purchased from Decon Laboratories. TOPO was purified by the fractional distillation method.²² All other chemicals were used as received.

Synthesis of MnSb nanoparticles in the presence of NaBH₄

The synthetic method for production of solution-phase MnSb nanoparticles in the presence of NaBH₄ was developed by modification of our previously reported MnSb nanoparticle synthesis method.⁷ TOPO (4.0 g), Ph₃Sb (1 mmol), Mn₂(CO)₁₀ (0.6-1.5 mmol), NaBH₄ (0.53-2.64 mmol), and 1-ODE (20.0 mL) were combined together in a Schlenk flask in the glove box and moved to a Schlenk line in a fume hood. The Schlenk flask was evacuated for about 20 min at 60 °C followed by purging with argon (Ar) to degas the mixture. The flask was heated using a heating mantle controlled by a programmable temperature

controller with a thermocouple placed directly in the solution. The contents were slowly heated (20 °C/10 min) up to 180 °C under Ar to avoid volatilization of $\text{Mn}_2(\text{CO})_{10}$, and then the temperature was rapidly increased up to 250 °C and maintained for 3-8 h. Upon heating, the initial light yellow color solution gradually turned into orange, red, dark red and black. The final black product was allowed to cool naturally to room temperature. The product was dispersed in chloroform and precipitated with ethanol, followed by centrifugation. This process was repeated several times, and then the product was dried under vacuum to obtain a free-flowing powder.

Study of Morphological Transformation

Near-stoichiometric amounts of $\text{Mn}_2(\text{CO})_{10}$ (0.6 mmol), Ph_3Sb (1 mmol), along with TOPO (4.0 g), 1-ODE (20.0 mL) and NaBH_4 (0.92 mmol) were initially employed, and the contents of the flask were slowly heated under Ar following the procedure described above for the synthesis of MnSb nanoparticles. After allowing the reaction to run for 3 h at 250 °C, a fraction (0.2 mL) was taken out and quenched in cold chloroform for Powder X-Ray Diffraction (PXRD) and Transmission Electron Microscopy (TEM) analyses. Immediately after taking out the fraction, $\text{Mn}_2(\text{CO})_{10}$ (0.9 mmol) heated and dissolved in 1-ODE (<10.0 mL) was cannulated into the initial reactant mixture at 250 °C under inert conditions. The contents were further heated for 3-8 h at 250 °C. The resultant black solution was then purified and isolated using the method described above. PXRD and TEM analysis were carried out to determine any phase or morphology differences, respectively.

Characterization

Powder X-Ray Diffraction

Room temperature Powder X-Ray Diffraction (PXRD) patterns were acquired in the range $2\theta = 20^\circ\text{--}70^\circ$ on a Bruker Phaser II model X-ray diffractometer equipped with a Cu anode. Samples were placed on a zero background quartz holder for measurements.

Transmission Electron Microscopy

Transmission Electron Microscopy (TEM) images were obtained on a JEOL 2010 transmission electron microscope operated at 200 kV. The specimens were prepared by dispersing the solid sample with sonication in chloroform and supporting the particles on a 200 mesh Cu grid coated with a carbon film.

High Angle Annular Dark Field- Scanning Transmission Electron Microscopy

The elemental composition of individual nanoparticles was analyzed using an FEI Titan 80-300 High Angle Annular Dark Field- Scanning Transmission Electron Microscope (HAADF-STEM) with ChemiSTEM technology at 200 kV.

Magnetic Measurements

Magnetic measurements were acquired on solid MnSb nanoparticle powders stored in a silica gel capsule under inert conditions up until the time of measurement in order to avoid oxidation. Magnetization (M) vs applied magnetic field (H) data were acquired using a Quantum Design Superconducting Quantum Interference Device (SQUID) magnetometer (MPMS-5S) at 50 K and 300 K, sweeping fields from +10,000 Oe to -10,000 Oe. All data are normalized to moles of Mn in the sample, determined by Inductively Coupled Plasma – Mass Spectrometry (ICP-MS).

Inductively Coupled Plasma – Mass Spectrometry (ICP-MS)

The elemental ratio of Mn:Sb and number of moles of Mn were obtained using an Agilent 7700x Series ICP-MS. Solid powders of MnSb nanoparticles (~1 mg, weighed on an analytical balance) were completely dissolved in concentrated nitric acid (2 mL) and then diluted to 100 mL in a volumetric flask with 2% nitric acid (HNO_3) (v/v). This was further diluted by taking a 0.10 mL aliquot and diluting to 100 mL using 2% HNO_3 . 2% HNO_3 served as the blank solution. In order to calibrate the instrument, Mn and Sb standard solutions (300, 500, 700, 1200, 1500, 1800, 2500 ppb) were prepared by a serial dilution of Mn and Sb stock solutions.

Results and Discussion

Effect of NaBH_4 Addition on MnSb Nanoparticle Synthesis with Near-Stoichiometric $\text{Mn}_2(\text{CO})_{10}$: In order to test our hypothesis, *i.e.*, the introduction of a reducing agent eliminates the need for excess $\text{Mn}_2(\text{CO})_{10}$ to avoid co-precipitation of Sb, discrete MnSb nanoparticles were synthesized in the presence of NaBH_4 (0.53 mmol) by heating at 250°C using a slight excess of $\text{Mn}_2(\text{CO})_{10}$ (1.2 mmol Mn: 1.0 mmol Sb) in TOPO and 1-ODE for a dwell time of 3 hr. **Fig. 1** shows the difference between the two MnSb nanoparticle syntheses carried out using near-stoichiometric $\text{Mn}_2(\text{CO})_{10}$ in the absence and presence of NaBH_4 .

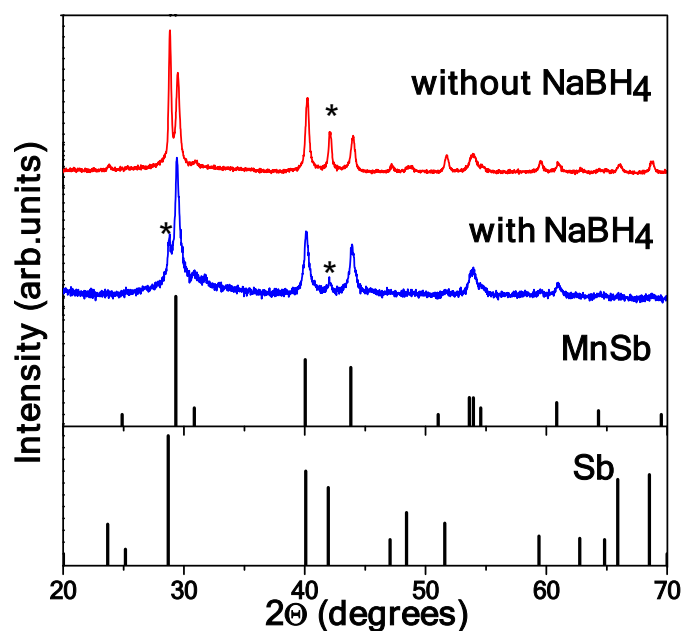


Figure 1: PXRD data of the product of MnSb synthesis carried out in the absence and in the presence of NaBH_4 (0.53 mmol). The corresponding peaks for Sb, (012) at $2\theta=28.7$ and (110) at $2\theta=42$, are marked with asterisks for comparison. (MnSb-PDF # 03-065-0388, Sb-PDF # 00-035-0732)

The addition of NaBH_4 clearly results in less elemental Sb formation and also, based on diffraction peak broadening, smaller MnSb nanoparticles. Assuming that the remaining Sb precipitate could be avoided by an increase of the amount of NaBH_4 , we increased the amount of reductant incrementally from 0.53 to 2.64 mmol,

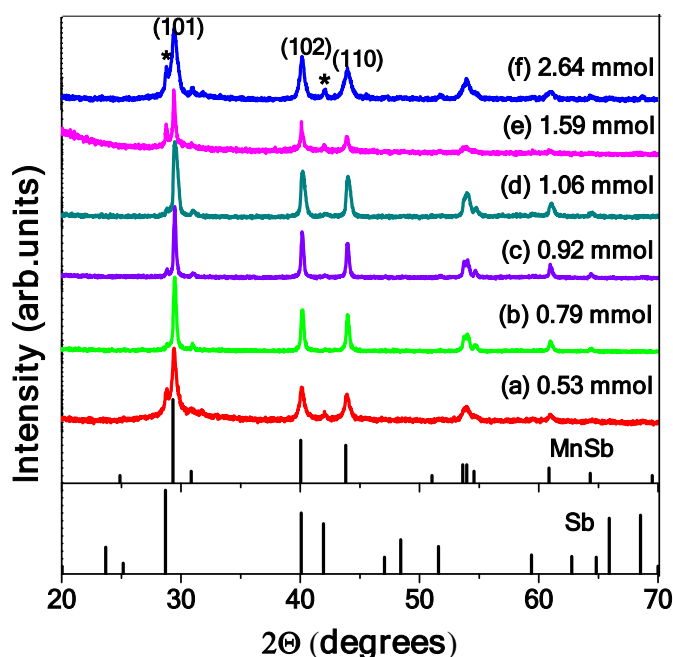


Figure 2: PXRD data of the product of MnSb synthesis (1 mmol Sb and 1.2 mmol Mn) as a function of added NaBH_4 . The asterisk denotes the position of elemental Sb; the principal peaks of MnSb are labeled. (MnSb-PDF # 03-065-0388, Sb-PDF # 00-035-0732).

keeping the concentrations of Mn and Sb unchanged.

According to **Fig. 2 a, b**, the increase of NaBH_4 up to 0.79 mmol continues to decrease Sb precipitation (qualitatively determined by the intensity ratio of (012) and (110) [marked with asterisks] of the Sb phase to (101) and (110) peaks [as labelled] of the MnSb phase). However, complete elimination of Sb is not observed. The quantity remains small but constant up through 1.06 mmol (**Fig. 2 c, d**) whereas for higher NaBH_4 concentrations (1.59 – 2.64 mmol) the amount of Sb is again increased (**Fig. 2 e, f**)

Scherrer size calculations of the crystallite size of the MnSb nanoparticles for different NaBH_4 amounts (0.53, 0.79, 0.92, 1.06, 1.59, 2.64 mmol), when measured from either MnSb (101) peak, or the MnSb (110) (when significant peak overlap of MnSb (101) with Sb (012) occurs), are presented in **Table 1** and compared to values for the Sb impurity phase..

Table 1: The crystallite size of MnSb and Sb nanoparticles, synthesized using different NaBH₄ amounts, calculated by Scherrer equation²³

NaBH ₄ amount (mmol)	Crystallite size of MnSb from the (101) peak (nm)	Crystallite size of MnSb from the (110) peak (nm)	Crystallite size of Sb from the Sb (110) peak (nm)
0.53	*	16	66
0.79	*	40	**
0.92	22	23	**
1.06	43	36	37
1.59	34	35	54
2.64	*	25	39

* Crystallite size cannot be calculated due to peak overlap

** Crystallite size cannot be calculated due to the low intensity of the peak

In cases where the (101) peak can be resolved, the crystallite sizes are similar to values obtained from the MnSb (110) peak. However, there is no clear trend observed in crystallite size for MnSb and/or Sb vs NaBH₄ amount.

The challenges in computing crystallite size based on Scherrer equation become evident upon evaluation of TEM data. **Fig. 3** and **4** shows the TEM images of the MnSb samples corresponding to the PXRD patterns displayed in **Fig. 2**. Clearly, the introduction of NaBH₄ has had a profound effect on the morphology, resulting in tadpole-shaped particles, and rendering the Scherrer calculation for spherical nanoparticles inappropriate. According to **Fig. 3** and **4** all the nanoparticles synthesized by the addition of NaBH₄ possess a head-tail morphology rather than the spherical morphology characteristic of MnSb when no NaBH₄ is included.⁷

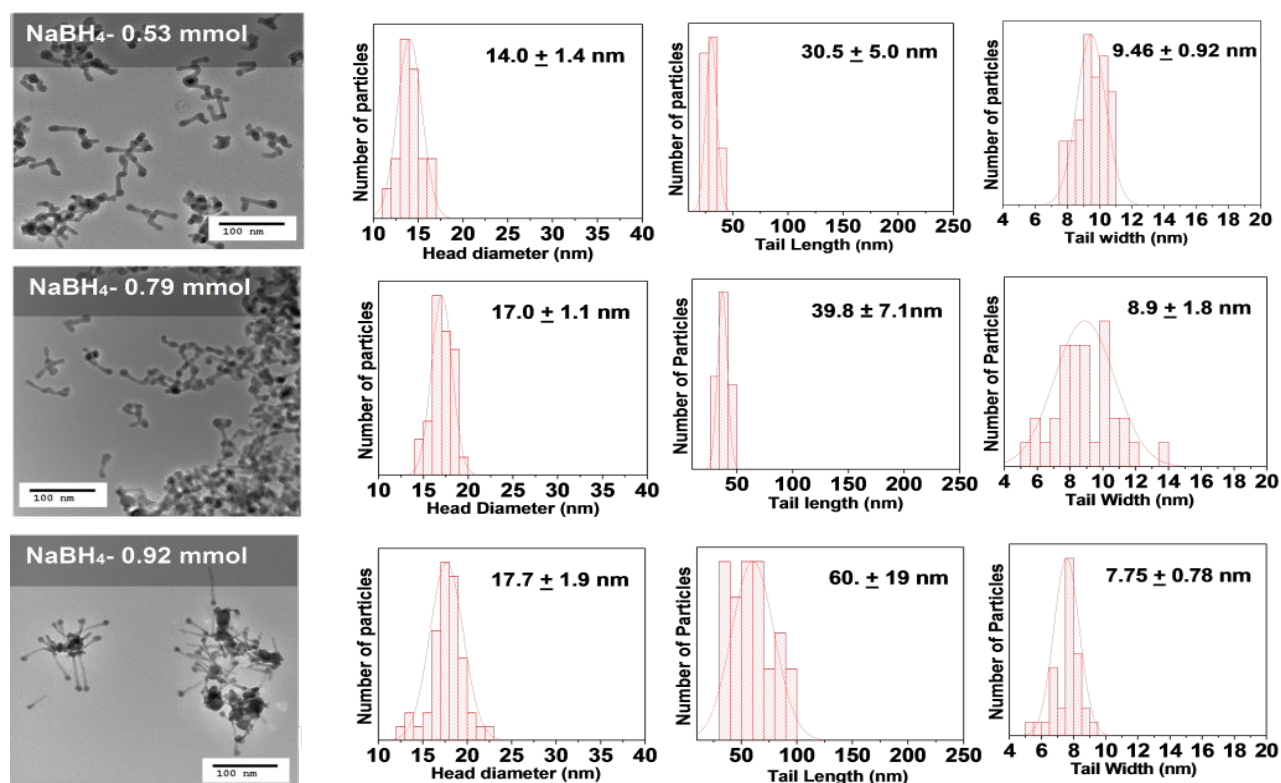


Figure 3: TEM images of MnSb syntheses in the presence of different amounts of NaBH₄ (0.53-0.92 mmol) and associated histograms corresponding to the head diameter, tail length, and tail width.

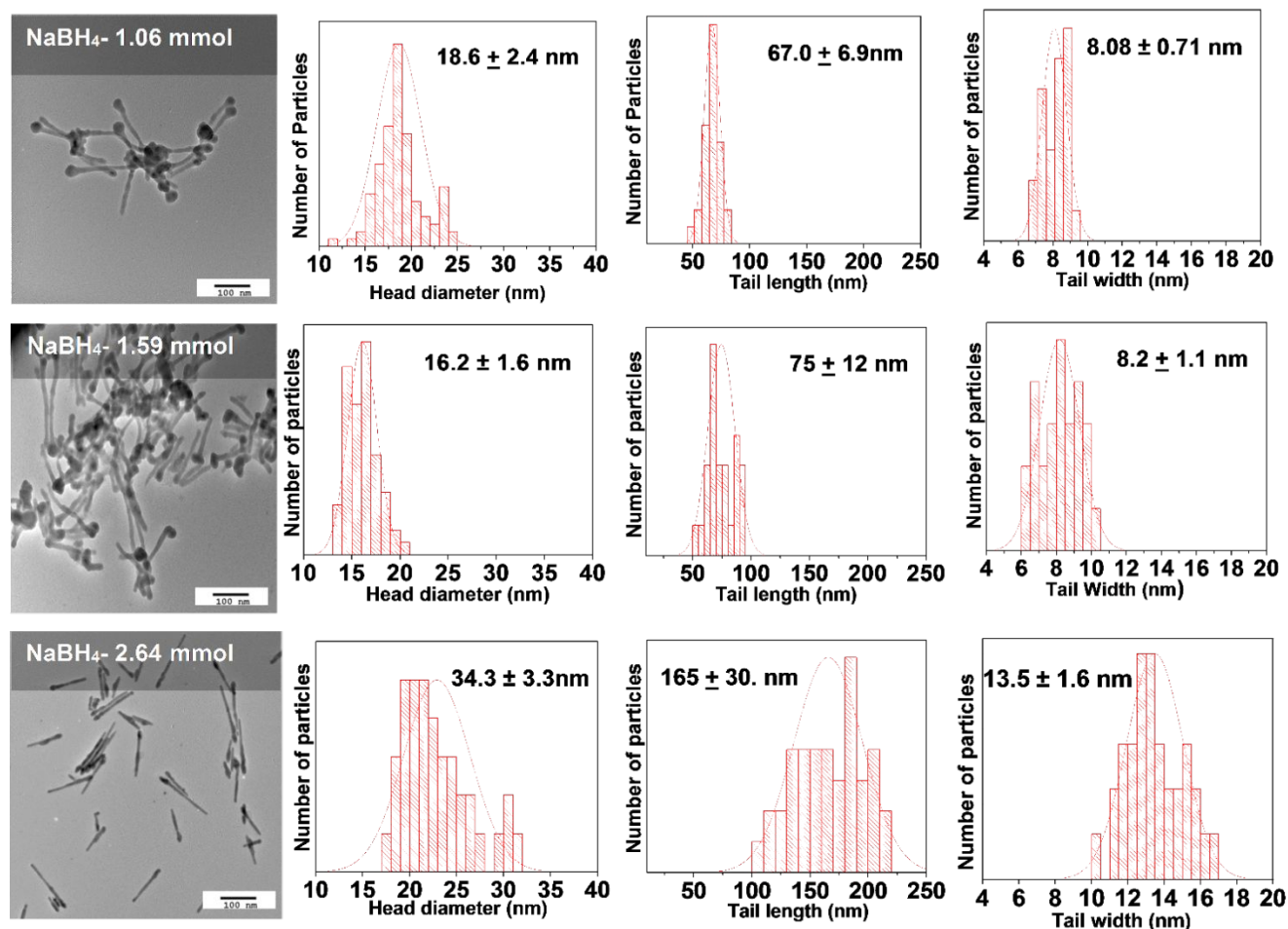


Figure 4: TEM images of MnSb syntheses in the presence of different amounts of NaBH₄ (1.06-2.64 mmol) and associated histograms corresponding to the head diameter, tail length, and tail width

However, except in the case of 2.64 mmol of NaBH₄, the size of the head is relatively constant (*ca.* 14-19 nm) in diameter as is the tail width (*ca.* 8-10 nm) throughout the different NaBH₄ values used. In contrast, the tail part lengthens gradually with the addition of NaBH₄, from 30 to 100 nm, resulting in elongated head-tail nanoparticles. When the NaBH₄ amount is 2.64 mmol the former spherical-shaped head becomes oval in shape, *ca.* 35 nm, (head diameter measured along the direction of the tail), the diameter swells to 13 nm and the length extends to 165 nm.

Chemical Nature of the Head-Tail Morphology:

In order to probe the compositional heterogeneity, the elemental mapping of individual head-tail particles was obtained from HAADF-STEM

imaging combined with elemental analysis (EDS) as shown in **Fig. 5**. **Fig. 5 a-c** reveals the presence of Mn and Sb elements throughout the particle, from head to tail. However, when considering the distribution of Mn and Sb in the line scan (**Fig. 5 g**), Sb is slightly rich in the head region, while both Mn and Sb are co-localized in the tail region. Elemental mapping of individual particles was also done for O, P and B to check for incorporation of these elements (**Fig. 5 d, e**) and **Fig S1, ESI#**). According to the HAADF-STEM data, oxygen is present throughout the particle, which we presume is due to surface oxidation or a shell of MnO_x. However, the MnO_x shell appears thinner (< 1 nm) than in the nanoparticles synthesized in the absence of NaBH₄ (*ca.* 2 nm).⁷ The mapping data do not indicate co-localization of B despite its small

atomic size (Fig S1, ESI#), but P is evident throughout the head-tail morphology (Fig. 5 g). Based on these data, we conclude that the nanoparticles are composed of an Sb-rich MnSb head and a MnSb tail, with a small amount of P throughout the structure. According to the ICP-MS

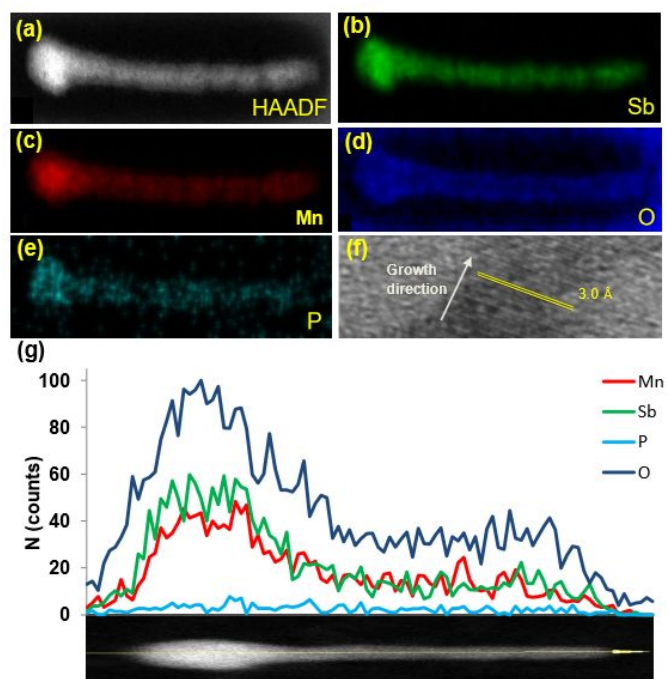


Figure 5: (a) HAADF-STEM of MnSb nanoparticles synthesized in the presence of NaBH₄ (2.64 mmol) and EDS mapping of (b) Sb and (c) Mn (d) O and (e) P; (f) Bottom mount image of a portion of the tail part of a MnSb nanoparticle showing lattice fringes; (g) line scan elemental analysis of a single head-tail MnSb nanoparticle: :Sb (green), Mn (red), O (blue), and P (cyan).

analysis, the P content is 0.2% of the total atomic composition, consistent with minimal uptake. This P may correspond to either the presence of surface bound TOPO, the stabilizing agent that protects the particles from aggregation, or incorporation of P into the nanoparticle lattice during the synthesis. According to previous studies of MnAs nanoparticles reported by our group, unintentional incorporation of P into nanoparticles of as high as a few percent can occur when TOPO is used. This incorporation takes place during the nucleation step, and then P is lost due to a self-purification process.²⁴ We surmise a similar process is going on

in the MnSb synthesis. From ICP-MS data analysis, the Mn:Sb ratio of the overall particle was 1:1.08. This excess Sb presence can be either attributed to MnSb + Sb, MnSb_{1+δ} or as a concentration gradient of Mn and Sb, as is observed in CdS_{1-x}Se_x nanorods.²⁵ However, the presence of peaks corresponding to elemental Sb in the PXRD (Fig. 2) suggests MnSb + Sb is the more likely scenario. Note that Scherrer size calculations for Sb-grain sizes (ca 40-70 nm, Table 1) are not reflected in the TEM, likely due to sampling errors. Keeping in mind that a few larger crystallites will dominate the PXRD pattern, but may correspond to a small volume fraction, this is either not-captured during “snap-shots” acquired on the TEM grid, or the larger grains do not make it onto the grid at all (they settle out after sonication, and before application of solution to the grid).

Furthermore, some head-tail particles with ‘swollen areas’ in the tail were observed, particularly when the NaBH₄ amount becomes ≥1.59 mmol, reminiscent of peas in a pod (Fig. S2, ESI#). In order to analyze these ‘pea pods’, we took line scans along the horizontal and vertical axes of these tails, across the ‘swollen areas’. According to Fig. 6, the ‘swollen areas’ or ‘peas’ are richer in Sb relative to Mn and P, while in the non-swollen areas, both Mn and Sb have similar concentrations. Moreover, according to Fig. 6 b, the core is rich in Sb. Thus the ‘swollen areas’ are similar to the heads, representing Sb rich areas.

Mechanism of Formation and Transformation:

We posit that the anisotropic growth of nanoparticles arises from an SSS growth mechanism. Aliquots taken as a function of time reveal that at short times, ca. 30 min, the samples are heterogeneous, comprising short rods and spheres (Fig. S3, ESI#, 30 min). By 60 min the nanoparticle morphology mostly consists of tadpoles, and there is no significant morphology change at longer times (Fig. S3, ESI#, 60 - 180 min). At the same time, the PXRD data for all the samples (Fig. S3 ESI#) are very similar, with all patterns indicative of MnSb formation, but peak asymmetry in the (101) reflection suggests elemental Sb is also present. It has been reported in the literature that colloidal Sb nanocrystals can be rapidly (< 1 min) obtained by hot injection methods

at modest (150–200 °C) temperatures,²⁶ and these act as precursors for alloy²⁷ and composite^{28–29} formation. Moreover, it is known that superlattices of Mn and Sb spontaneously form epitaxial MnSb at the interface, (with lattices oriented along the $\langle 110 \rangle$ or $\langle 001 \rangle$ direction)³⁰; the latter is consistent with our observation of $\sim 3\text{Å}$ lattice spacing ((002) lattice plane) along the growth direction, **Fig. 5f**. Accordingly, a simple hypothesis would be that Mn solution species react with Sb nuclei generating MnSb nanorods oriented epitaxially along *c* with growth occurring at the head-tail interface: the SSS mechanism. However, the actual mechanism is likely more complex, as diffusion of Mn into the Sb nuclei forms a MnSb shell (see **Fig. 6**) from which the “tail” emerges at one end. Note that the SSS mechanism is chosen over Solution-Liquid-Solid (SLS) based on the high melting point (mp) of bulk Sb (mp: 630.6 °C) and MnSb (mp: 840 °C) relative to the synthesis temperature.

limiting reactant, then the more reductant added, the longer the rods should be (assuming a constant number of nuclei), which is exactly what we see. So, Sb nucleates, reacts with Mn to form MnSb, which grows as a rod because of the epitaxial relationship and the high precursor concentration. Note that head diameter and tail width does not change much with increasing NaBH_4 conc (ca 18 nm head diameter and 9 nm tail) until the concentration gets quite large. At this point the head diameter doubles, tail width increases by 50 % and length doubles. This is also where swollen Sb-rich features become apparent along the length of the particle. We surmise that MnSb is not stable to disproportionation to the elements for high reductant concentrations and that liberated antimony condenses to form nuclei within the structure (i.e., the swollen features). The fate of Mn is unclear, but it may be reconstituted as a reactive precursor. Thus, the ‘tail’ grows longer because the reactive Mn precursor concentration is higher, but this is superposed over a thickening of the ‘head’ and ‘tail’ to accommodate Sb nanoparticle nucleation and growth.

In an attempt to better understand how Mn and NaBH_4 concentrations dictate the formation mechanism and to probe whether the morphologies can be interconverted and excess Sb eliminated, a set of reactions was carried out in the presence of NaBH_4 (0.79 mmol), with the addition of 0.7, 0.9, and 1.5 mmol of $\text{Mn}_2(\text{CO})_{10}$ (i.e. 40, 80, 200% excess of moles, respectively). Note that 0.9 mmol is the $\text{Mn}_2(\text{CO})_{10}$ amount used in the successful synthesis of MnSb nanoparticles in the absence of a reducing agent.⁷ **Fig. 7** shows the corresponding TEM images. Interestingly, the morphology of the MnSb nanoparticles has evolved from the elongated head–tail (no excess $\text{Mn}_2(\text{CO})_{10}$) to contracted head-tail (0.7 mmol excess $\text{Mn}_2(\text{CO})_{10}$) and then spherical-shaped nanoparticles (≥ 0.9 mmol excess $\text{Mn}_2(\text{CO})_{10}$). Therefore, even in the presence of NaBH_4 , when there is a large excess of $\text{Mn}_2(\text{CO})_{10}$ the MnSb nanoparticles obtained are spherical in shape as is the case for MnSb nanoparticles reported previously. As shown in **Fig. S4 a ESI[†]** the PXRD pattern of the synthesis with 0.7 mmol of $\text{Mn}_2(\text{CO})_{10}$ is indicative of the MnSb phase; however, no conclusion can be drawn as to the presence or absence of a small amount of Sb

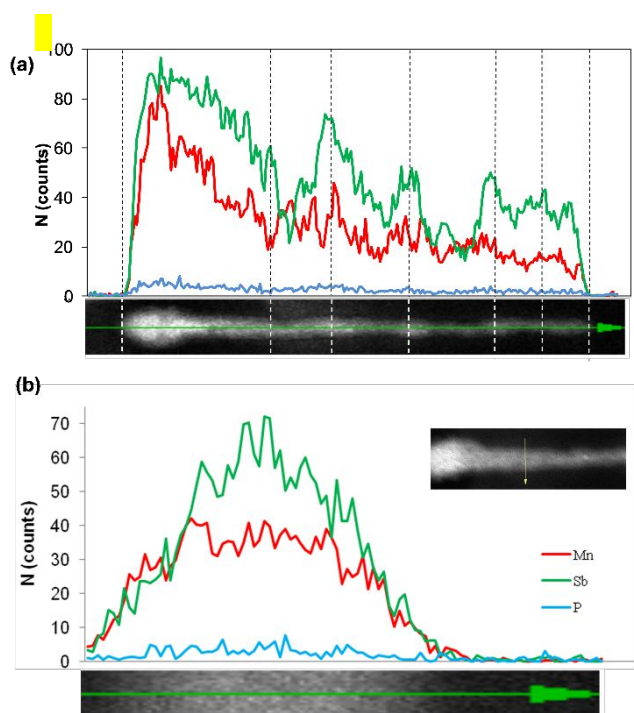


Figure 6: HAADF-STEM of a MnSb nanoparticle with a ‘swollen tail’ synthesized in the presence of 2.64 mmol of NaBH_4 and line scan elemental analysis (a) axial (b) vertical scan across the tail: Sb (green) Mn (red) and P (cyan).

We think it likely that the reductant also results in a higher concentration of reactive Mn in solution, which promotes tail growth. If reactive Mn is the

phase due to the breadth of the peak. Indeed, the asymmetry of the peak (unusually broad at the base) may suggest an amorphous component. In addition, the presence of crystalline MnO_2 was noted. The PXRD patterns of 0.9 mmol and 1.5 mmol of $\text{Mn}_2(\text{CO})_{10}$ do not have apparent oxide peaks (**Fig. S4, ESI[#]**) and if Sb is present, it is a minor product in relation to MnSb. Thus, spherical particles appear to form when Mn is present in excess and formation of elemental Sb is minimized.

Alternations between Two Morphologies: After seeing that there exist two different morphologies that correlate to the amount of $\text{Mn}_2(\text{CO})_{10}$ amounts (near-stoichiometric and excess), we sought to evaluate whether these two morphologies can be interchanged as a function of the $\text{Mn}_2(\text{CO})_{10}$ amount.

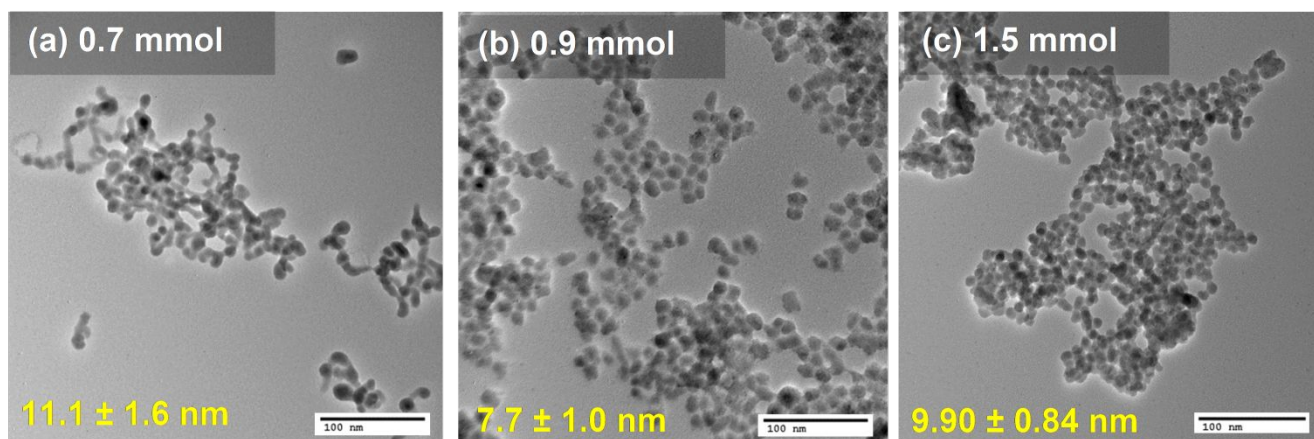


Figure 7 (a-c): TEM images of MnSb nanoparticles synthesized in the presence of NaBH_4 (0.79 mmol), using 0.7, 0.9, 1.5 mmol (40, 80, 200% mole excess) of $\text{Mn}_2(\text{CO})_{10}$ (particle diameter refers to the head diameter).

In order to do so, MnSb nanoparticles were synthesized by using near-stoichiometric reactant amounts in the presence of 0.79 mmol of NaBH_4 , and then excess $\text{Mn}_2(\text{CO})_{10}$ (0.9 mmol) in 1-ODE was introduced to the same reaction mixture and the morphology evolution probed as a function of time. **Fig. 8** shows how the elongated head-tail morphologies that arise under the near-stoichiometric reactant conditions progressively transform into spherical nanoparticles, when heated for different reaction times (3–5 h) at 250 °C.

According to **Fig. 8**, the initial head-tail nanoparticles having the head diameter *ca.* 16 nm and tail width *ca.* 9 nm formed in the presence of a slight excess of $\text{Mn}_2(\text{CO})_{10}$ relative to Ph_3Sb and

1.59 mmol of NaBH_4 (**Fig. 8 a, b**) turn into mixed spheres (diameter *ca.* 18 nm) and rods (width *ca.* 9 nm) 3 h after introduction of excess $\text{Mn}_2(\text{CO})_{10}$ (0.9 mmol). After 5 h reaction time almost all these mixed morphologies have converted to spherical-shaped nanoparticles with a diameter *ca.* 8 nm. As shown in **Fig. S5, ESI[#]** a minor amount of elemental Sb appears along with the majority MnSb phase in the presence of a near-stoichiometric $\text{Mn}_2(\text{CO})_{10}$ amount. However, this minor phase disappears upon the introduction of more $\text{Mn}_2(\text{CO})_{10}$ to the mixture and heating for an additional 3–8 h. A control experiment was carried out to determine whether this morphological transformation was actually an effect of additional $\text{Mn}_2(\text{CO})_{10}$ or an effect of extended reaction time.

An initial reaction mixture having near-stoichiometric $\text{Mn}_2(\text{CO})_{10}$ (0.6 mmol) was heated for 8 h at 250 °C. **Fig. S6, ESI[#]** shows the TEM images (low mag and high mag) and PXRD pattern of the reaction product. According to these TEM images, after an extended reaction time (8 h), the sample was still dominated by elongated head-tail nanoparticles or nanorods, with only a minute amount of spherical nanoparticles. The PXRD pattern indicates the presence of Sb (minor phase) and MnSb (major phase). This suggests that the main driver for the morphology is the $\text{Mn}_2(\text{CO})_{10}$ concentration relative to Ph_3Sb and NaBH_4 .

Based on the above observations, we surmise that in the presence of excess $\text{Mn}_2(\text{CO})_{10}$, elongated

MnSb nanoparticles transform into spherical nanoparticles. While the mechanism is not clear, we hypothesize that the narrow areas between two swollen Sb-rich islands, as shown in **Fig. 6a** and **8c**, are likely vulnerable to particle etching. Hence, the excess $\text{Mn}_2(\text{CO})_{10}$ in the solution can attach to the open facets and “pinch-off” a particle. Alternatively (or in addition) the shape may be related to surface energetics for manganese oxide shells, with thick shells dictating spherical geometry.

field-cooled data) in the range 245-255 K, but very small per-Mn moments (0.04 BM^7 vs. *ca* 3.5 BM^6 reported for bulk MnSb). The small moments were attributed to a large volume fraction of amorphous manganese oxide, motivating our study of the use of a reducing agent to limit oxide formation. Accordingly, the elongated MnSb head-tail nanoparticles synthesized under near-stoichiometric $\text{Mn}_2(\text{CO})_{10}$ and in the presence of 0.79 mmol NaBH_4 were evaluated for comparison.

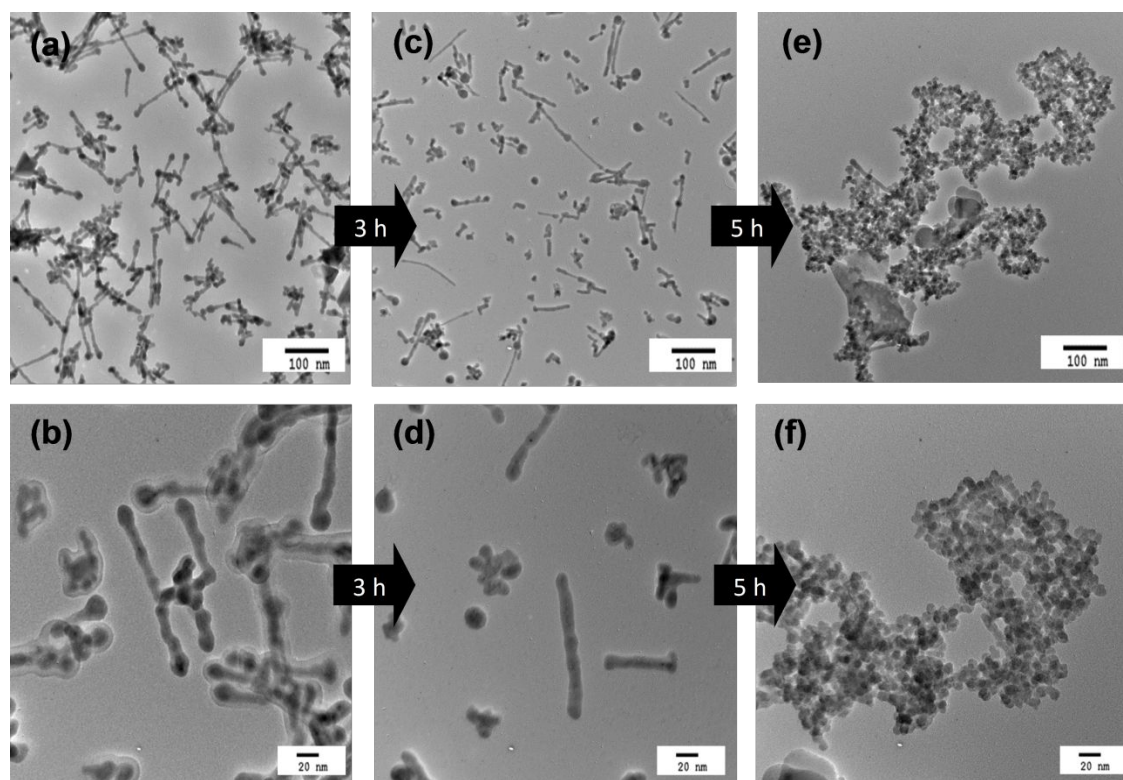


Figure 8: Low and high magnification TEM images showing the transformation of initial elongated head-tail nanorods, [(a) (low mag), (b) (high mag)] into mixed head-tail nanorod and spherical nanoparticles 3h after adding 0.9 mmol of $\text{Mn}_2(\text{CO})_{10}$ [(c) (low mag), (d) (high mag)] and into spherical nanoparticles after 5 h total [(e) (low mag), (f) (high mag)].

Magnetic Properties of the Elongated Head-Tail vs Spherical MnSb Nanoparticles: Our prior studies established that MnSb nanoparticles prepared with excess Mn and without NaBH_4 are ferromagnetic, as expected, with $T_c > 340\text{K}$ (operating limit of our instrument; bulk MnSb has a T_c of 572K) with superparamagnetic blocking temperature (T_B , obtained from zero-field and

Fig. 9 (a) shows the magnetization per mole of Mn (M) vs applied magnetic field (H) data obtained at 50 K . Additionally, M vs. H data were acquired on nanoparticles prepared with excess $\text{Mn}_2(\text{CO})_{10}$, respectively, also in the presence of 0.79 mmol NaBH_4 , and are shown in **Fig. 9b**. It is evident

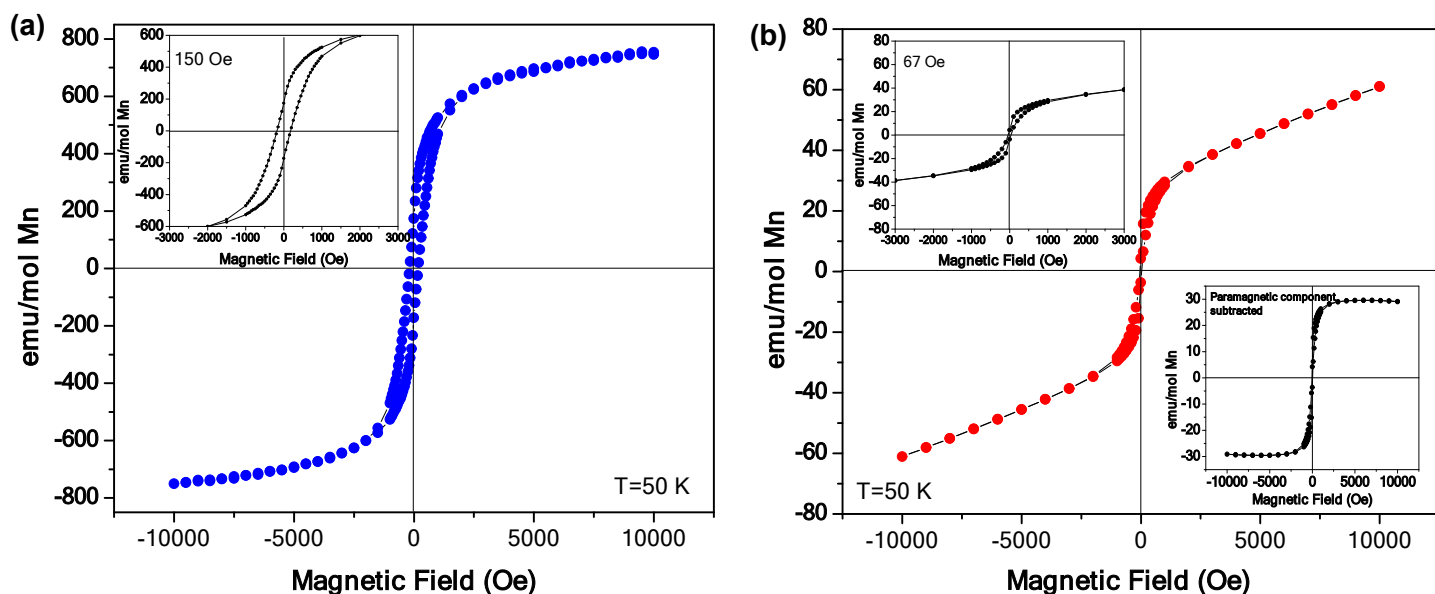


Figure 9: Field dependence of the DC molar magnetization (M) (normalized to Mn moles) recorded at different magnetic fields (H) at 50 K for MnSb nanoparticles synthesized (a) with near-stoichiometric $\text{Mn}_2(\text{CO})_{10}$ amount (0.6 mmol) and (b) with excess $\text{Mn}_2(\text{CO})_{10}$ (1.5 mmol) in the presence of 1.0 mmol of Ph_3Sb and 0.79 mmol NaBH_4 (250 °C for 3 h). The top insets show an enlarged image of the loops of the hysteresis curve obtained at 50 K; the bottom inset in Fig 9(b) shows that curve after subtraction of paramagnetic background component

from comparison of Fig. 9 a, b that the sample prepared with near-stoichiometric Mn has a larger moment (saturation magnetization) than the one with excess Mn. Additionally, there is also a significant paramagnetic component when excess Mn is present, as indicated by the linearity in the M vs H at higher field in Fig. 9b. Subtracting this component yields the M vs H curve shown in the lower inset of Fig. 9b from which an estimated ferromagnetic moment of 0.04 BM/mol Mn is obtained for the ca 8 nm spherical particles, the same as obtained in our prior study. Thus, regardless of the inclusion of NaBH_4 in the reaction, in all cases where Mn is present in excess, a significant reduction in ferromagnetic MnSb occurs. In contrast, when Mn concentration is limited and NaBH_4 is present, a moment of 0.8 BM/mol Mn is obtained, consistent with our original hypothesis. Using this value as representative of “nanoscale MnSb”, we can compute the relative moment of the ferromagnetic (presumably MnSb, 0.8 BM) to paramagnetic

portion of the sample in Fig. 9b. These data suggest that >75% by mass of MnSb samples prepared with excess Mn is attributable to a paramagnetic phase, most likely an amorphous oxide. Applying this formulation, in our ca ~8 nm particles, the ferromagnetic MnSb core would be ~5 nm in diameter.

In addition, there is also evidence for a second magnetic phase in samples prepared with excess Mn. Note that in the case of the near-stoichiometric $\text{Mn}_2(\text{CO})_{10}$ amount, the hysteresis loop reflects a coercivity of ca. 150 Oe. In contrast, for the sample prepared with excess $\text{Mn}_2(\text{CO})_{10}$ the hysteresis loop is much narrower, indicative of a coercivity of ca. 67 Oe. Moreover, with excess Mn, the hysteresis loop demonstrates a small asymmetry, a thinning of the loop (*goose-neck* effect) close to zero applied field. We attributed this previously to metamagnetism;⁷ however, in the absence of evidence for metamagnetism in bulk MnSb, it is more likely that the asymmetry is indicative of a second magnetic phase.³¹⁻³²

As the samples in Fig 9 a, b were prepared under different conditions, we cannot discern whether the differences in magnetic response are a function of morphology or just reflect the relative volumes of crystalline MnSb. However, we can say that while the morphology of the samples prepared in the presence of NaBH₄ with near-stoichiometric Mn is complex, the magnetism is fairly simple and indicative of MnSb as the only magnetic phase (albeit with 25% of the expected moment). In contrast, with excess Mn where well-formed spherical particles are produced, there appear to be two ferromagnetic contributors (both minor), and the major product is paramagnetic.

Conclusion

The addition of NaBH₄ into the previously reported MnSb nanoparticle system eliminates the necessity of adding an excess amount of Mn₂(CO)₁₀ that can compensate for the adventitious oxygen source that leads to MnO_x. This approach changes the particle morphology into elongated head-tail structures, in which the heads are slightly rich in Sb, and the tail composed of more or less equal amounts of Mn and Sb. The formation of these head-tail morphologies can be explained by the Solution-Solid-Solid (SSS) growth mechanism, in which Sb-rich Mn-Sb clusters serve as solid catalysts that trigger the formation of the MnSb tail along the <001> direction. We also show that there is a morphological transformation between the elongated head-tail nanoparticles and spherical shape nanoparticles upon introduction of more Mn₂(CO)₁₀ into the previously prepared head-tail nanoparticles. The saturation magnetic moment of these head-tail nanoparticles is about twenty times higher (0.8 BM/MnSb) compared to the saturation magnetic moment of previously reported spherical shape MnSb nanoparticles, or the ones reported herein prepared with excess Mn. We expect that the discovery of SSS growth mechanism for antimonides will enable targeting of some challenging, but important ternary phase nanoparticle systems such as MnNiSb, MnPdSb, MnGa₂Sb₂.³³ The synthesis of these phases, and further elucidation of the formation mechanism, is the subject of current investigations.

Conflicts of interest

The authors declare no conflicts of interest

Acknowledgements

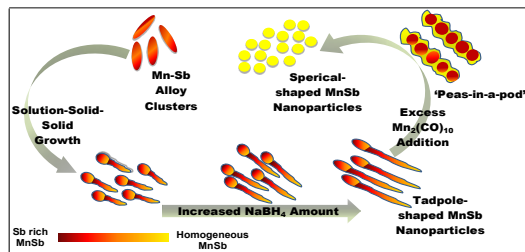
The work was supported by National Science Foundation (NSF) through grant NSF DMR-1361470. This work made use of the JEOL 2010 TEM supported by NSF award number 0216084 and the PXRD facility supported by NSF award number 1427926. HAADF-STEM data were acquired at the North Carolina State University MAH acknowledges a Rumble Fellowship. We thank Karena Chapman for useful discussion and preliminary pair distribution function analysis data, and Dr. Yang Liu from North Carolina State University for conducting line scanning and elemental mapping data.

References

1. Tegus, O.; Brück, E.; Buschow, K. H. J.; de Boer, F. R., Transition-metal-based magnetic refrigerants for room-temperature applications. *Nature*, **2002**, *415* (6868), 150.
2. Mira, J.; Rivadulla, F.; Rivas, J.; Fondado, A.; Guidi, T.; Caciuffo, R.; Carsughi, F.; Radaelli, P.; Goodenough, J., Structural Transformation Induced by Magnetic Field and "Colossal-Like" Magnetoresistance Response above 313 K in MnAs. *Phys. Rev. Lett.* **2003**, *90* (9), 097203.
3. Mizuguchi, M.; Akinaga, H.; Ono, K.; Oshima, M., Crystallographic and magneto-optical studies of nanoscaled MnSb dots grown on GaAs. *Appl. Phys. Lett.* **2000**, *76* (13), 1743-1745.
4. Zhang, H.; Kushvaha, S.; Chen, S.; Gao, X.; Qi, D.; Wee, A.; Wang, X.-S., Synthesis and magnetic properties of MnSb nanoparticles on Si-based substrates. *Appl. Phys. Lett.* **2007**, *90* (20), 202503.
5. Burrows, C. W.; Dobbie, A.; Myronov, M.; Hase, T. P.; Wilkins, S. B.; Walker, M.; Mudd, J. J.; Maskery, I.; Lees, M. R.; McConville, C. F., Heteroepitaxial growth of ferromagnetic MnSb (0001) films on Ge/Si (111) virtual substrates. *Cryst. Growth Des.* **2013**, *13* (11), 4923-4929.
6. Henini, M., *Molecular beam epitaxy: from research to mass production* (Edition 1) Newnes: **2012**, 480-482.

7. Hettiarachchi, M. A.; Abdelhamid, E.; Nadgorny, B.; Brock, S. L., Synthesis of colloidal MnSb nanoparticles: consequences of size and surface characteristics on magnetic properties. *J. Mater. Chem. C.*, **2016**, *4* (28), 6790-6797.
8. Wang, J.; Chen, K.; Gong, M.; Xu, B.; Yang, Q., Solution–Solid–Solid Mechanism: Superionic Conductors Catalyze Nanowire Growth. *Nano Lett.*, **2013**, *13* (9), 3996-4000.
9. Guria, A. K.; Sarkar, S.; Patra, B. K.; Pradhan, N., Efficient superionic conductor catalyst for solid in solution–solid–solid growth of heteronanowires. *J. Phys. Chem. Lett.*, **2014**, *5* (4), 732-736.
10. Zhang, Y.; Shen, S.; Wang, Q., Controllable growth of Ag₂S–CdS heteronanostructures. *CrystEngComm*, **2014**, *16* (40), 9501-9505.
11. Trentler, T. J.; Hickman, K. M.; Goel, S. C.; Viano, A. M.; Gibbons, P. C.; Buhro, W. E., Solution-liquid-solid growth of crystalline III-V semiconductors: an analogy to vapor-liquid-solid growth. *Science*, **1995**, *270* (5243), 1791-1794.
12. Wang, F.; Dong, A.; Sun, J.; Tang, R.; Yu, H.; Buhro, W. E., Solution– liquid– solid growth of semiconductor nanowires. *Inorg. Chem.*, **2006**, *45* (19), 7511-7521.
13. Wang, F.; Wayman, V. L.; Loomis, R. A.; Buhro, W. E., Solution–Liquid–Solid Growth of Semiconductor Quantum-Wire Films. *ACS Nano* **2011**, *5* (6), 5188-5194.
14. Wang, F.; Dong, A.; Buhro, W. E., Solution–Liquid–Solid Synthesis, Properties, and Applications of One-Dimensional Colloidal Semiconductor Nanorods and Nanowires. *Chem. Rev.* **2016**, *116* (18), 10888-10933.
15. Wang, J.; Yang, C.; Huang, Z.; Humphrey, M. G.; Jia, D.; You, T.; Chen, K.; Yang, Q.; Zhang, C., Seed-catalyzed heteroepitaxial growth and nonlinear optical properties of zinc selenide nanowires. *J. Mater. Chem.*, **2012**, *22* (19), 10009-10014.
16. Li, Q.; Zou, C.; Zhai, L.; Zhang, L.; Yang, Y.; Chen, X. a.; Huang, S., Synthesis of wurtzite CuInS₂ nanowires by Ag₂S-catalyzed growth. *CrystEngComm*, **2013**, *15* (9), 1806-1813.
17. Connor, S. T.; Hsu, C.-M.; Weil, B. D.; Aloni, S.; Cui, Y., Phase transformation of biphasic Cu₂S– CuInS₂ to monophasic CuInS₂ nanorods. *J. Am. Chem. Soc.*, **2009**, *131* (13), 4962-4966.
18. Han, W.; Yi, L.; Zhao, N.; Tang, A.; Gao, M.; Tang, Z., Synthesis and shape-tailoring of copper sulfide/indium sulfide-based nanocrystals. *J. Am. Chem. Soc.*, **2008**, *130* (39), 13152-13161.
19. Zhu, G.; Xu, Z., Controllable growth of semiconductor heterostructures mediated by bifunctional Ag₂S nanocrystals as catalyst or source-host. *J. Am. Chem. Soc.*, **2010**, *133* (1), 148-157.
20. Geng, X.; Liu, H.; Zhai, L.; Xiong, Z.; Hu, J.; Zou, C.; Dong, Y.; Yang, Y.; Huang, S., Colloidal synthesis of CuGaS_xSe_{2-x} nanoribbons mediated by Cu_{1.75}(SSe) nanocrystals as catalysts. *J. Alloy. Compd.*, **2014**, *617*, 961-967.
21. Zou, C.; Li, M.; Zhang, L.; Yang, Y.; Li, Q.; Chen, X. a.; Xu, X.; Huang, S., Ag₂S-catalyzed growth of quaternary AgInZn₇S₉ semiconductor nanowires in solution. *CrystEngComm*, **2011**, *13* (10), 3515-3520.
22. Wang, F.; Tang, R.; Kao, J. L.-F.; Dingman, S. D.; Buhro, W. E., Spectroscopic identification of tri-n-octylphosphine oxide (TOPO) impurities and elucidation of their roles in cadmium selenide quantum-wire growth. *J. Am. Chem. Soc.*, **2009**, *131* (13), 4983-4994.
23. Scherrer, P., Determination of the size and internal structure of colloidal particles using X-rays. *Nachr. Ges. Wiss. Göttingen*, **1918**, *2*, 98-100.
24. Pimmachcharige, R.; Zhang, Y.; Regmi, R.; Lawes, G.; Brock, S. L., Solution-phase growth mechanism of phosphorus-doped MnAs nanoparticles: size, polydispersity and dopant control on the nanoscale. *J. Mater. Chem. C.*, **2017**, *5* (13), 3352-3358.
25. Ruberu, T. P. A.; Vela, J., Expanding the One-Dimensional CdS–CdSe Composition Landscape: Axially Anisotropic CdS_{1-x}Se_x Nanorods. *ACS Nano* **2011**, *5* (7), 5775-5784.
26. He, M.; Kravchuk, K.; Walter, M.; Kovalenko, M. V., Monodisperse antimony nanocrystals for high-rate Li-ion and Na-ion battery anodes: nano versus bulk. *Nano Lett.*, **2014**, *14* (3), 1255-1262.
27. He, M.; Walter, M.; Kravchuk, K. V.; Erni, R.; Widmer, R.; Kovalenko, M. V., Monodisperse SnSb nanocrystals for Li-ion and Na-ion battery anodes: synergy and dissonance between Sn and Sb. *Nanoscale* **2015**, *7* (2), 455-459.
28. Walter, M.; Erni, R.; Kovalenko, M. V., Inexpensive antimony nanocrystals and their composites with red phosphorus as high-performance anode materials for Na-ion batteries. *Sci. Rep.* **2015**, *5*, 8418.
29. Liang, L.; Xu, Y.; Wen, L.; Li, Y.; Zhou, M.; Wang, C.; Zhao, H.; Kaiser, U.; Lei, Y., Hierarchical Sb-Ni nanoarrays as robust binder-free anodes for high-performance sodium-ion half and full cells. *Nano Res.*, **2017**, *10* (9), 3189-3201.
30. Moritani, I.; Nakayama, N.; Shinjo, T., X-ray diffraction study of Mn/Sb multilayered films with artificial superstructures. *J. Phys. Condens. Matter.*, **1990**, *2* (49), 9717.

31. Ramírez-Camacho, M.; Sánchez-Valdés, C.; Gervacio-Arciniega, J.; Font, R.; Ostos, C.; Bueno-Baques, D.; Curiel, M.; Sánchez-Llamazares, J.; Siqueiros, J.; Raymond-Herrera, O., Room temperature ferromagnetism and ferroelectricity in strained multiferroic BiFeO₃ thin films on La_{0.7}Sr_{0.3}MnO₃/SiO₂/Si substrates. *Acta Mater.*, **2017**, *128*, 451-464.
32. Raghunathan, A.; Melikhov, Y.; Snyder, J.; Jiles, D., Modeling of two-phase magnetic materials based on Jiles–Atherton theory of hysteresis. *J. Magn. Magn. Mater.*, **2012**, *324* (1), 20-22.
33. Bocarsly, J. D.; Levin, E. E.; Garcia, C. A.; Schwennicke, K.; Wilson, S. D.; Seshadri, R., A simple computational proxy for screening magnetocaloric compounds. *Chem. Mater.*, **2017**, *29* (4), 1613-1622.



Novel synthetic route to synthesize solution-phase anisotropic MnSb nanoparticles was developed and the Solution-Solid-Solid growth mechanism was elucidated.